Supporting Information

Selective and High-Rate CO_2 Electroreduction by Metal-Doped Covalent Triazine Frameworks: A Computational and Experimental Hybrid Approach

Shintaro Kato,[a] Takuya Hashimoto,[a] Kazuyuki Iwase,[b] Takashi Harada,[a] Shuji Nakanishi,*[a,c] and Kazuhide Kamiya*[a,c]

[a] *Research Center for Solar Energy Chemistry, Graduate School of Engineering Science, Osaka University, 1-3 Machikaneyama, Toyonaka, Osaka 560-8531, Japan. E-mail: nakanishi@chem.es.osaka-u.ac.jp; kamiya.kazuhide.es@osaka-u.ac.jp*

[b] *Institute of Multidisciplinary Research for Advanced Materials, Tohoku University, 2-1-1 Katahira, Aoba-ku, Sendai, Miyagi 980-8577, Japan.*

[c] *Innovative Catalysis Science Division, Institute for Open and Transdisciplinary Research Initiatives, Osaka University, Suita, Osaka 565-0871, Japan.*

Experimental procedures

Synthesis of *M*-CTFs

The preparation of CTF has been described in detail in our previous publications.[1] Briefly, a mixture of 2,6-pyridinedicarbonitrile (129 mg, Sigma-Aldrich), $ZnCl_2$ (1.37 g, Wako), and Ketjen Black EC600JD (129 mg, Lion) were placed in a vacuum-sealed glass ampoule that was subsequently heated at 400 °C for 40 h. The obtained CTF powder was sequentially washed with distilled water, 1 M hydrochloric acid, tetrahydrofuran (Wako), and acetonitrile. CTF samples were modified with each metal (Co, Cu, Fe, Ni, Ru, in addition to Ag and Sn) using an impregnation method in a 10 mM metal chloride ($CoCl_2$, $CuCl_2$, $FeCl_3$, $NiCl_2$, or $RuCl_3$) aqueous solution at 80 °C for 3 h. The resultant powder was washed with distilled water and dried. Ag-CTF was synthesized using an impregnation method in 0.1 mM CH_3COOAg aqueous solution at 80 °C for 3 h. Sn-CTF was synthesized using an impregnation method in 0.1 mM $SnCl_2$ anhydrous ethanol solution in a glovebox at room temperature for 3 h because $SnCl_2$ is hygroscopic and easily aggregates into Sn(OH)Cl particles in dilute aqueous solution.[2]

Electrochemical measurements

All electrochemical experiments were performed using an electrochemical workstation (HZ-7000, Hokuto Denko). Three-chamber electrochemical cells in which two electrolyte compartments were separated by a Nafion membrane (Sigma-Aldrich, Nafion 117) were used (Fig. S21). A Pt wire and Ag/AgCl/KCl(sat.) electrode were used as the counter and reference electrodes, respectively. Electrode potentials were rescaled to the RHE reference with IR correction. The flow rate of CO_2 was set at 15 mL/min. The CO_2 reduction activity was evaluated with a 1 M $KHCO_3$ electrolyte solution (pH 8.6). The catalyst ink was prepared by dispersing 4.5 mg *M*-CTF in a mixture of 387 µL isopropanol and 13 µL Nafion solution (5 wt%, Sigma-Aldrich) using a homogenizer; the resultant ink was then added dropwise onto a GDE (GDL38BC, Sigracet, catalyst area: ~0.5 cm^2) on a hotplate at 80 °C. The catalyst loading on the GDE was controlled to be ~9.0 mg/cm^2. We confirmed that the CO_2RR activities for M-CTFs did not depend on the ionomer and counter electrodes in our electrochemical measurements (Fig. S10 and S14).

Characterization

Sample surfaces were inspected by field-emission scanning electron microscopy (FE-SEM; Hitachi, S-5000). XPS spectra (Axis Ultra, Kratos Analytical) were acquired using monochromatic Al Kα X-rays with $h\nu$ = 1486.6 eV. HR-TEM and EDX analyses were conducted using a spherical aberration-corrected TEM system (ARM-200F, JEOL). Ni and Sn K-edge XAFS spectra were acquired at the BL01B1 beamline station at SPring-8 at the Japan Synchrotron Radiation Research Institute. A double-crystal Si(111) monochromator for the Ni-CTF and a Si(311) monochromator for the Sn-CTF were used to obtain X-ray absorption spectroscopy data. The measurements for the as-prepared *M*-CTFs and the reference materials were conducted in transmission mode, and those for the M-CTF/GDEs (*M* = Ni, Sn) before and after electrolysis were conducted in fluorescence yield mode using 19-element Ge solid-state detectors. EXAFS spectra were analyzed using the ATHENA and ARTEMIS software package.[3] Fourier transformation of EXAFS spectra was conducted over the *k*-space range 3–12 Å for the *M*-CTF powders and reference samples. FT-EXAFS analysis of the *M*-CTF/GDEs was conducted over the *k*-space range 3–10.5 Å for the Ni-CTF/GDE and 3–12 Å for the Sn-CTF/GDE because of the lower metal content of the GDE samples.

Analysis of CO_2RR products

The gas products were analyzed using a gas chromatograph (GC 2030, Shimazu, Japan), which was equipped with both a thermal conductivity detector (TCD) and a flame ionization detector. The gas chromatograph, in which He was used as the carrier gas, was equipped with a MICROPACKED ST column. The liquid products were quantified using nuclear magnetic resonance (NMR) spectroscopy (Varian 500 MHz, Agilent). ^{1}H NMR spectra of freshly acquired samples were collected using the water suppression mode reported elsewhere.[4] A 0.3 mL sample of the electrolyte after electrolysis was mixed with 0.3 mL of D_2O (Wako) containing dimethyl sulfoxide (DMSO; Wako) as an internal standard.

Density functional theory calculations

Structure relaxation was performed using the *PHASE/0*[5] code with a projector-augmented wave (PAW) pseudopotential.[6] We used the generalized gradient approximation of the Perdew–Burke–Ernzerhof model[7,8] with van der Waals (D3) correction.[9] The cutoff energy for the plane-wave function was set to 25 Rydberg, and the Brillouin zone was sampled using a 2 × 2 × 1 Monkhorst–Pack *k*-point set.[10,11] The atomic relaxations were conducted until the maximum force on all units was less than 0.05 eV/Å. The residual minimization method-direct inversion in the iterative subspace (RMM-DIIS) method[12-14] that considers spin polarization was used in the self-consistent field method.

M-CTFs and the corresponding slab models were constructed on the basis of a single CTF layer to simplify the calculation. The vacuum space was set to 15 Å to eliminate the interactions between the CTF layers. The formation energy of reaction intermediates (COOH*, CO*, H*) calculated by DFT (ΔE_{DFT}) was defined by the following equations:

$$\Delta E_{\mathrm{COOH}} = E_{\mathrm{COOH*}} - E_{*} - E_{\mathrm{CO2}} - \frac{1}{2}E_{\mathrm{H2}}$$

$$\Delta E_{\mathrm{CO}} = E_{\mathrm{CO*}} - E_{*} - E_{\mathrm{CO}}$$

$$\Delta E_{\mathrm{H}} = E_{\mathrm{H*}} - E_{*} - \frac{1}{2}E_{\mathrm{H2}}$$

where E_{ads*}, E_*, and E_{sub} denote the total energy of the system after adsorption, the total energy of the *M*-CTF, and the total energy of the substrate molecules, respectively. The Gibbs free energies of the CO_2RR intermediates in electrochemical reaction pathways were calculated on the basis of the CHE model proposed by Nørskov et al.[15] In this model, the chemical potential of the H^+/e^- pair, $G(H^+ + e^-)$, is equal to one-half of the chemical potential of gaseous hydrogen at a potential of 0 V vs. standard hydrogen electrode. Therefore, the formation Gibbs free energies of each intermediate were calculated using the following equations:

$$\Delta G_{COOH} = G_{COOH*} - G_* - G_{CO2} - \frac{1}{2}G_{H2}$$

$$\Delta G_{CO} = G_{CO*} - G_* - G_{CO}$$

$$\Delta G_{H} = G_{H*} - G_* - \frac{1}{2}G_{H2}$$

The free energy of each chemical state was calculated by the following equation:

$$G = E_{DFT} + E_{ZPE} - TS$$

where E_{DFT}, E_{ZPE} and TS are the total energy obtained from DFT calculations, zero-point energy corrections, and the entropy differences, respectively. The values for E_{ZPE} and TS were obtained from previous reports. The external potential could shift the free Gibbs energy of the reaction by $-eU$. In the present study, the solvation energy was not applied. When calculating the Gibbs free energy of CO, an energy correction of −0.51 eV was considered as a limitation of the PBE model.[16]

Table S1. Calculated values for free energy diagrams in Fig. 1(d) in the main paper (at −0.98 V).

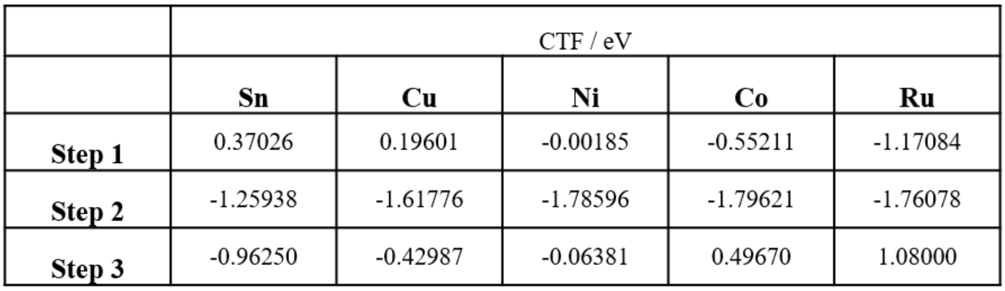

	CTF / eV				
	Sn	**Cu**	**Ni**	**Co**	**Ru**
Step 1	0.37026	0.19601	-0.00185	-0.55211	-1.17084
Step 2	-1.25938	-1.61776	-1.78596	-1.79621	-1.76078
Step 3	-0.96250	-0.42987	-0.06381	0.49670	1.08000

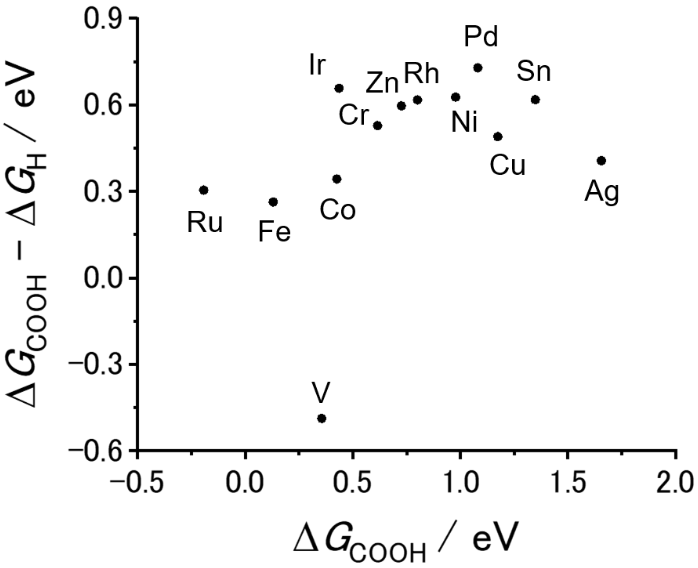

Fig. S1 ΔG_{COOH} - ΔG_H expressed in terms of ΔG_{COOH} for each *M*-CTF.

Table S2. Stabilization energy ($E_{\text{stabilize}}$) of *M*-CTFs.

	Fe	**Co**	**Ni**	**Cu**	**Ru**	**Rh**	**Pd**	**Ag**	**Sn**	**Ir**
$\boldsymbol{E}_{\textbf{stabilize}}$ [eV]	-2.55	-3.57	-4.25	-2.43	-4.55	-4.31	-2.14	-1.66	-3.10	-4.40

$E_{\text{stabilize}}$ was defined by the following equation:

$$E_{\text{stabilize}} = E(M\text{–support}) - E(\text{support}) - E(M_{\text{single}})$$

where $E(M\text{–support})$, $E(\text{support})$, and $E(M_{\text{single}})$ show the total energy of a metal-doped support (metal-doped CTFs), the energy of the support without metal modifications (CTFs), and the energy of single-metal atoms in vacuum, respectively.[17-20]

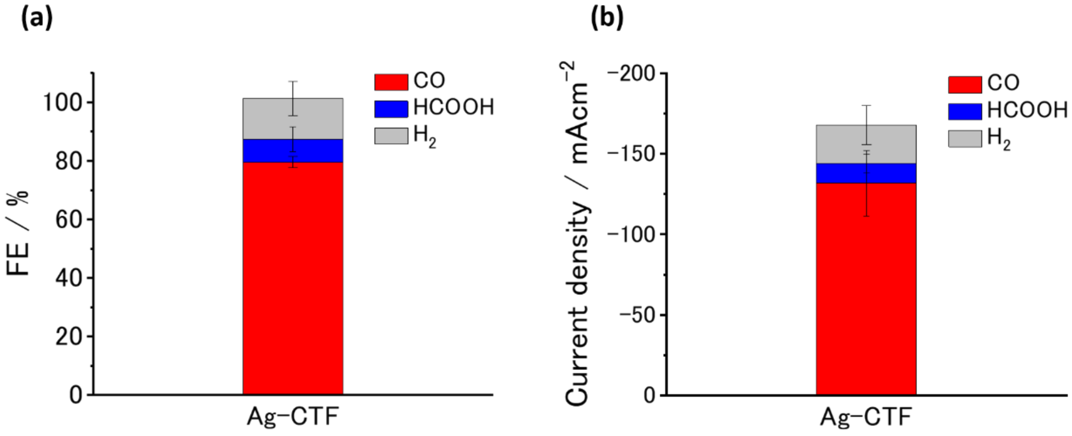

Fig. S2 (a) FE, (b) current density breakdown for products of CO_2 electrolysis in presence of Ag-CTF. Potential: -0.9 V vs. RHE; electrolyte: 1 M $KHCO_3$(aq) (pH 8.6).

Table S3. Metal atomic concentrations of *M*-CTFs, as determined by XPS analysis.

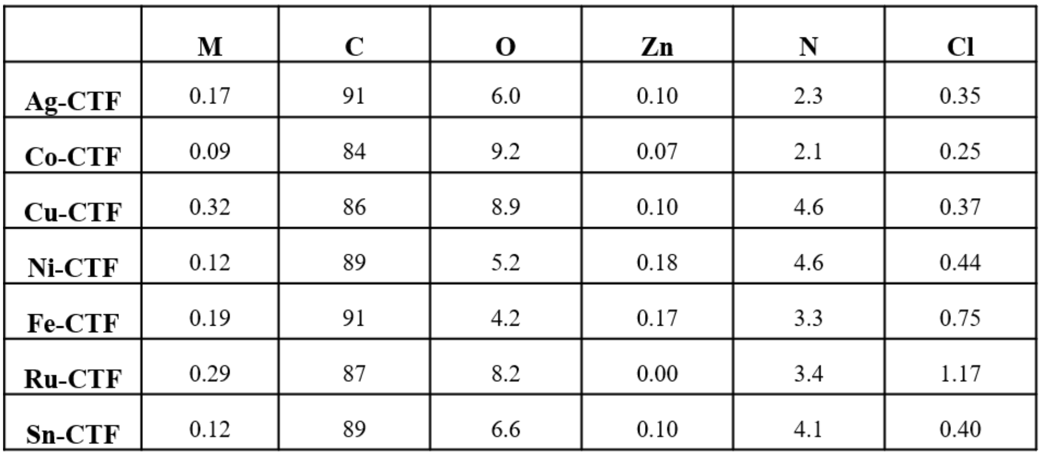

	M	C	O	Zn	N	Cl
Ag-CTF	0.17	91	6.0	0.10	2.3	0.35
Co-CTF	0.09	84	9.2	0.07	2.1	0.25
Cu-CTF	0.32	86	8.9	0.10	4.6	0.37
Ni-CTF	0.12	89	5.2	0.18	4.6	0.44
Fe-CTF	0.19	91	4.2	0.17	3.3	0.75
Ru-CTF	0.29	87	8.2	0.00	3.4	1.17
Sn-CTF	0.12	89	6.6	0.10	4.1	0.40

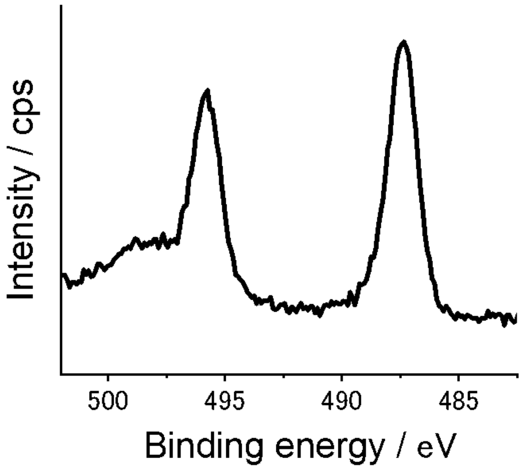

Fig. S3 Sn-3*d* XPS spectra for Sn-CTF. The Sn-3$d_{5/2}$ signal at 487 eV indicates that Sn^{IV} was dominant in the Sn-CTF.

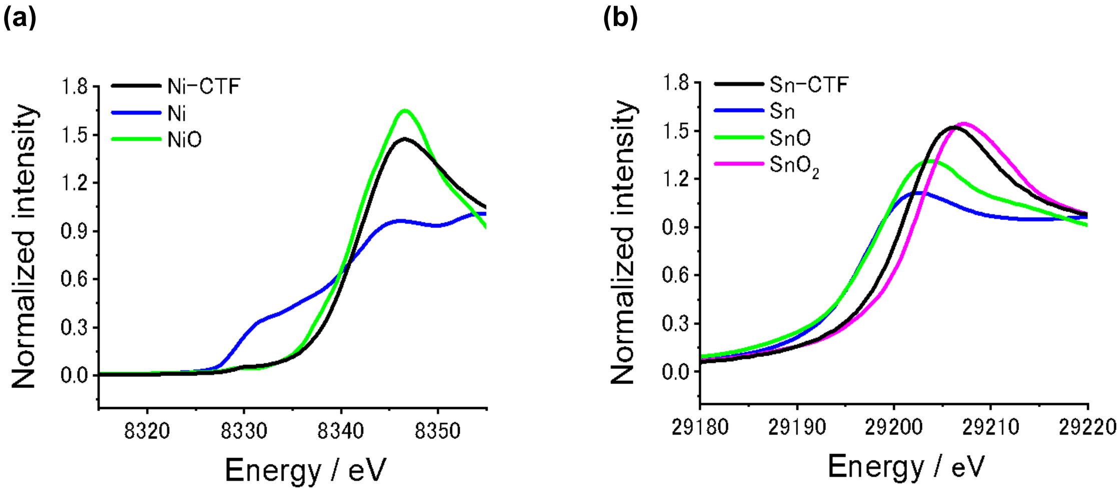

Fig. S4 XANES spectra of (a) Ni-CTF/GDE and (b) Sn-CTF/GDE. The black line shows the spectra of the *M*-CTF/GDEs. These results indicate that Ni^{II} was dominant in the Ni-CTF, whereas Sn^{IV} was dominant in the Sn-CTF.

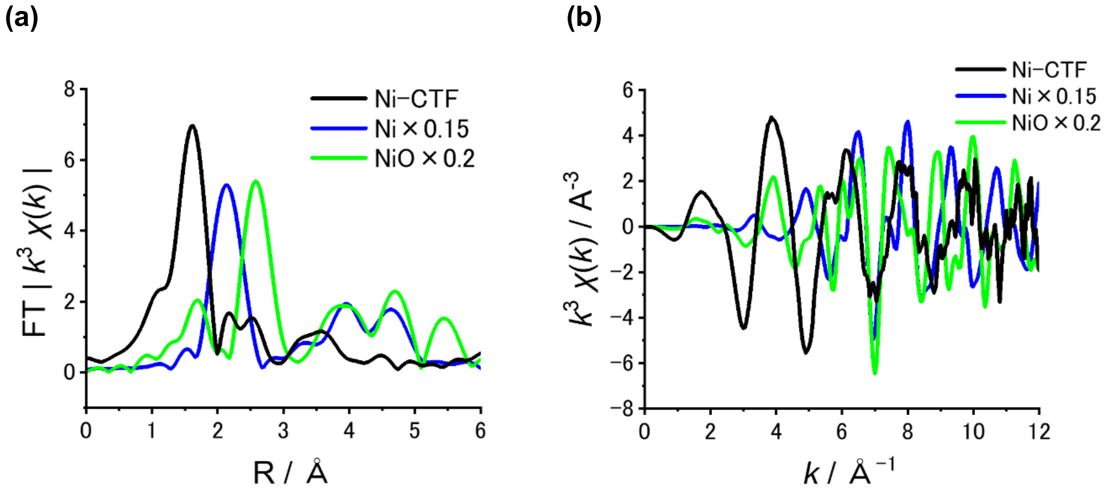

Fig. S5 (a) k^3-Weighted FT-EXAFS spectra and (b) k^3-weighted k-plot spectra of Ni-CTF and reference samples. Peaks corresponding to Ni–Ni bonds (2.1 Å) in Ni particles and Ni–O–Ni bonds (2.6 Å) in NiO were not observed.

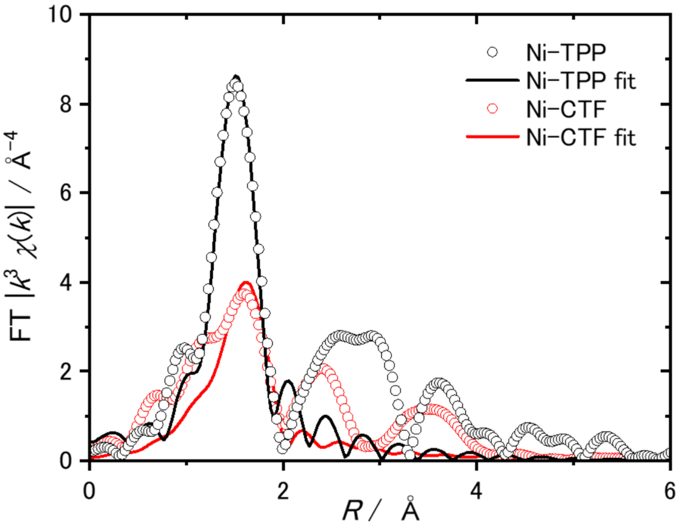

Fig. S6 FT-EXAFS spectra for the Ni-CTF and Ni-Tetraphenylporphyrin (Ni-TPP) powder. Black line and black dots represent the fitted and measured results for Ni-TPP, respectively. Red line and red dots represent the fitted and measured results for Ni-CTF, respectively. R-range used for fitting: 1−2.2 Å. Curve fitting for EXAFS spectra was conducted by using ARTEMIS software.[3]

Table S4. Results of curve fitting for EXAFS measurement.

	Bond Type	**CN**	**R**	**σ^2 (×10^{-3}, Å)**	**S_0^2**
Ni-TPP	Ni-N	4	1.93±0.02	3.3±2.0	1.03
Ni-CTF	Ni-N	3.4	2.07±0.05	8.9±4.6	1.03

R : atomic distance (Å), CN : coordination number, σ^2 : Debye–Waller factor, S_0^2 : Amplitude reduction factor.

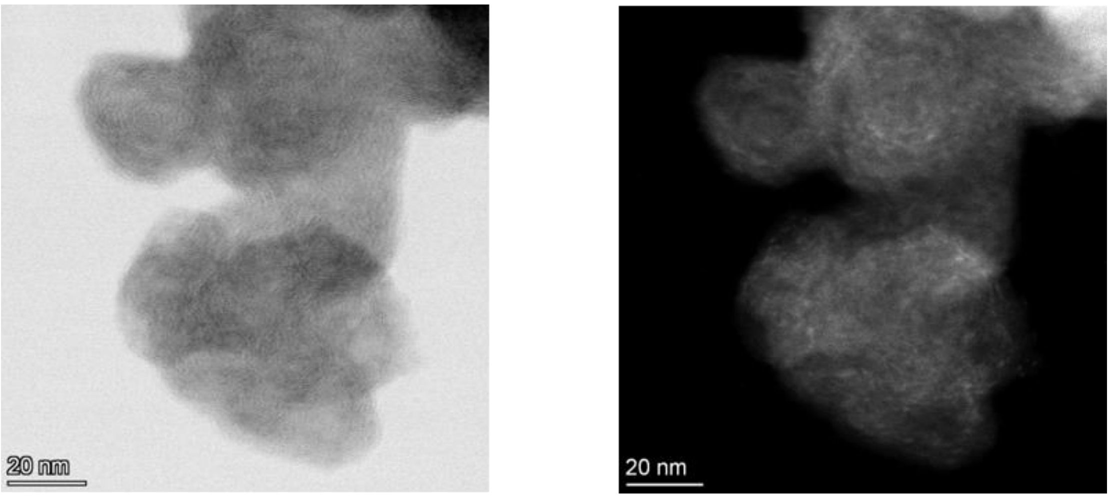

Fig. S7 HR-TEM image of Sn-CTF (left) and corresponding high-angle annular dark-field scanning image (right).

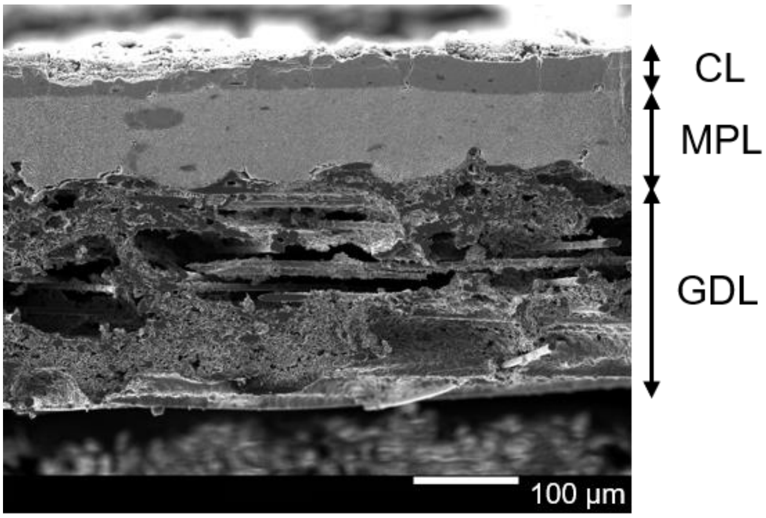

Fig. S8 Cross-sectional SEM image of Ni-CTF/GDE.

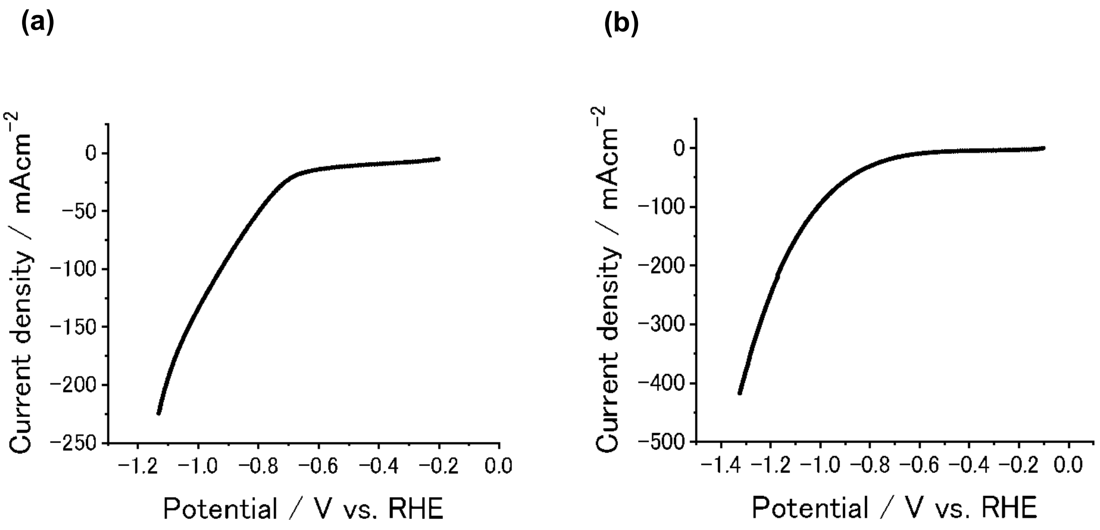

Fig. S9 Current density (*j*)–potential (*U*) curves for (a) Ni-CTF/GDE and (b) Sn-CTF/GDE. Electrolyte: 1 M $KHCO_3$(aq) (pH 8.6); scanning rate: 100 mV/s; surface area: 0.5 cm^2. The applied potential was controlled by 80% IR-compensation and converted to the reversible hydrogen electrode (RHE) scale.

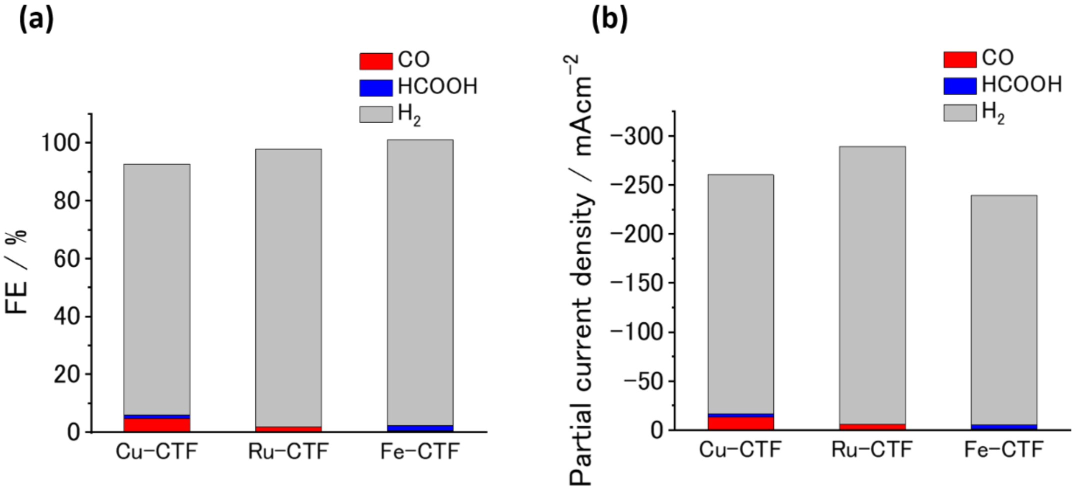

Fig. S10 (a) FE, (b) current density breakdown for products of CO_2 electrolysis in presence of *M*-CTFs (*M* = Cu, Ru, Fe) when Sustainion ionomer (anion exchange ionomer) was utilized instead of Nafion ionomer (cation exchange ionomer) to prepare catalyst inks. Potential: -0.9 V vs. RHE; electrolyte: 1 M $KHCO_3$(aq) (pH 8.6).

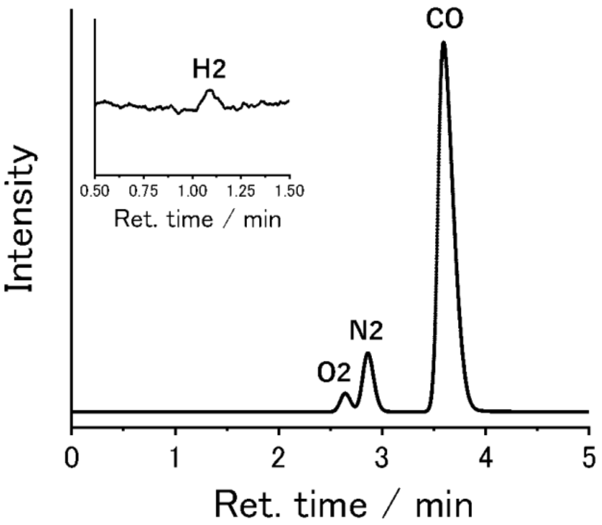

Fig. S11 Representative GC-TCD chart for Ni-CTF/GDE at −0.9 V vs. RHE for 10 min in 1 M $KHCO_3$(aq).

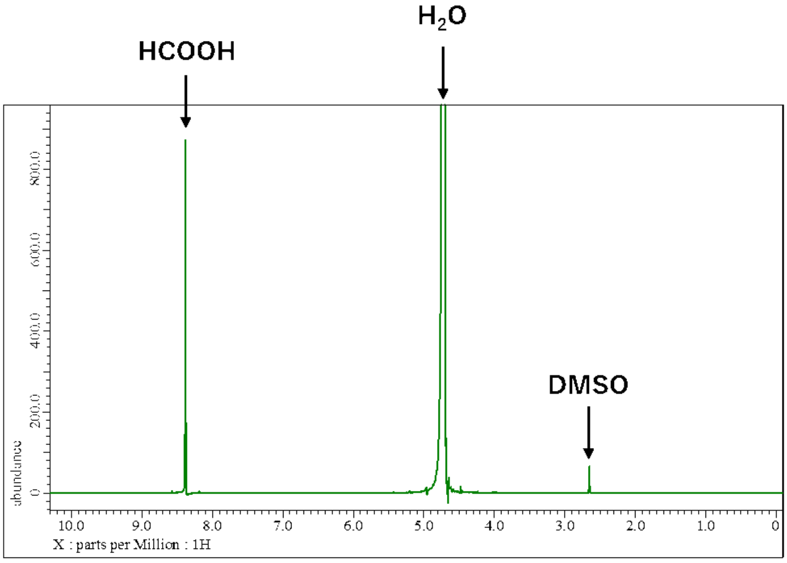

Fig. S12 ^{1}H NMR spectrum of liquid product corresponding to Sn-CTF/GDE at −0.9 V vs. RHE for 10 min. DMSO was added as an internal standard.

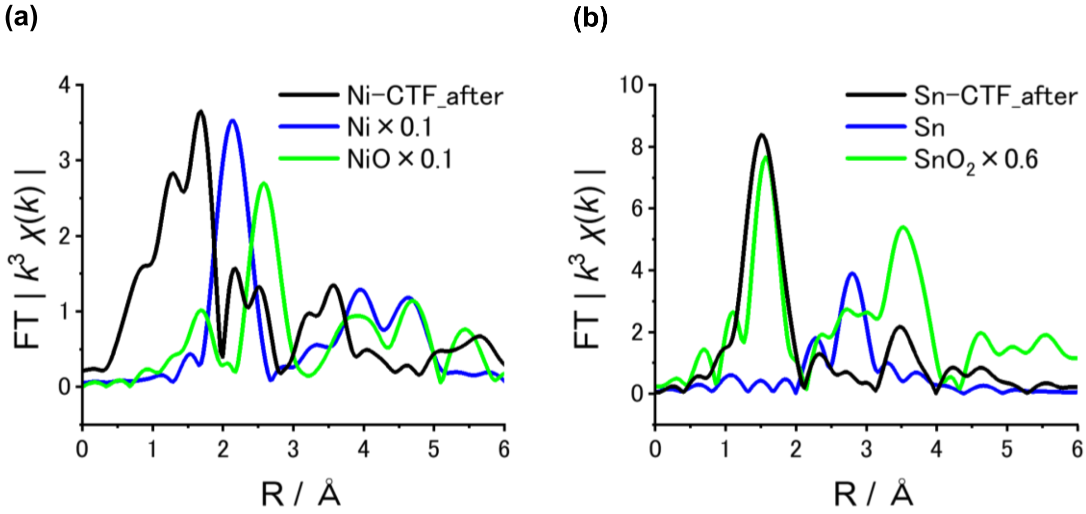

Fig. S13 k^3-Weighted FT-EXAFS spectra of (a) Ni K edge for the Ni-CTF/GDE after electrolysis and for reference samples and (b) Sn K edge for Sn-CTF/GDE after electrolysis and for reference samples.

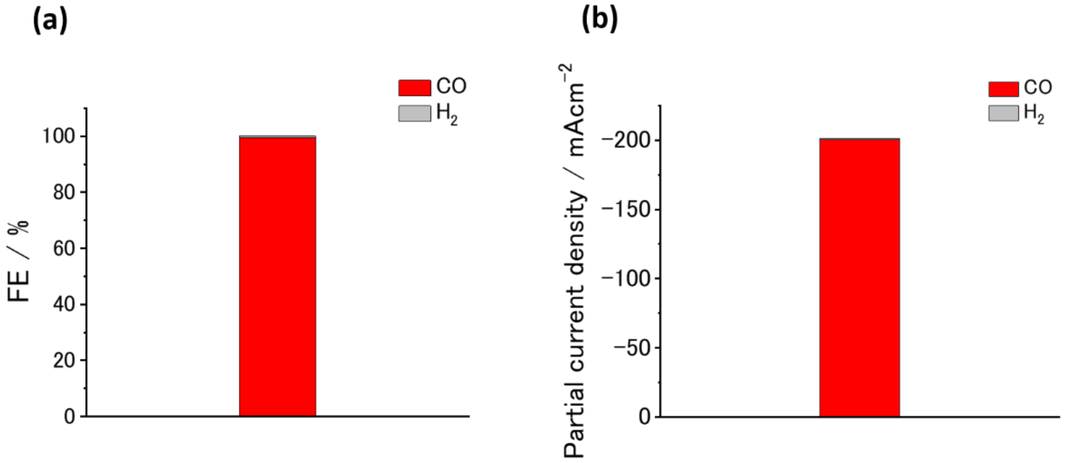

Fig. S14 (a) FE, (b) current density breakdown for products of CO_2 electrolysis in presence of Ni-CTF when IrO_2/Ti mesh anode (electrode area: 3.75 cm^2, porosity: 56 %, wire diameter: 20 µm, Tanaka Kikinzoku) was utilized instead of Pt wire anode. Potential: -0.9 V vs. RHE; electrolyte: 1 M $KHCO_3$(aq) (pH 8.6).

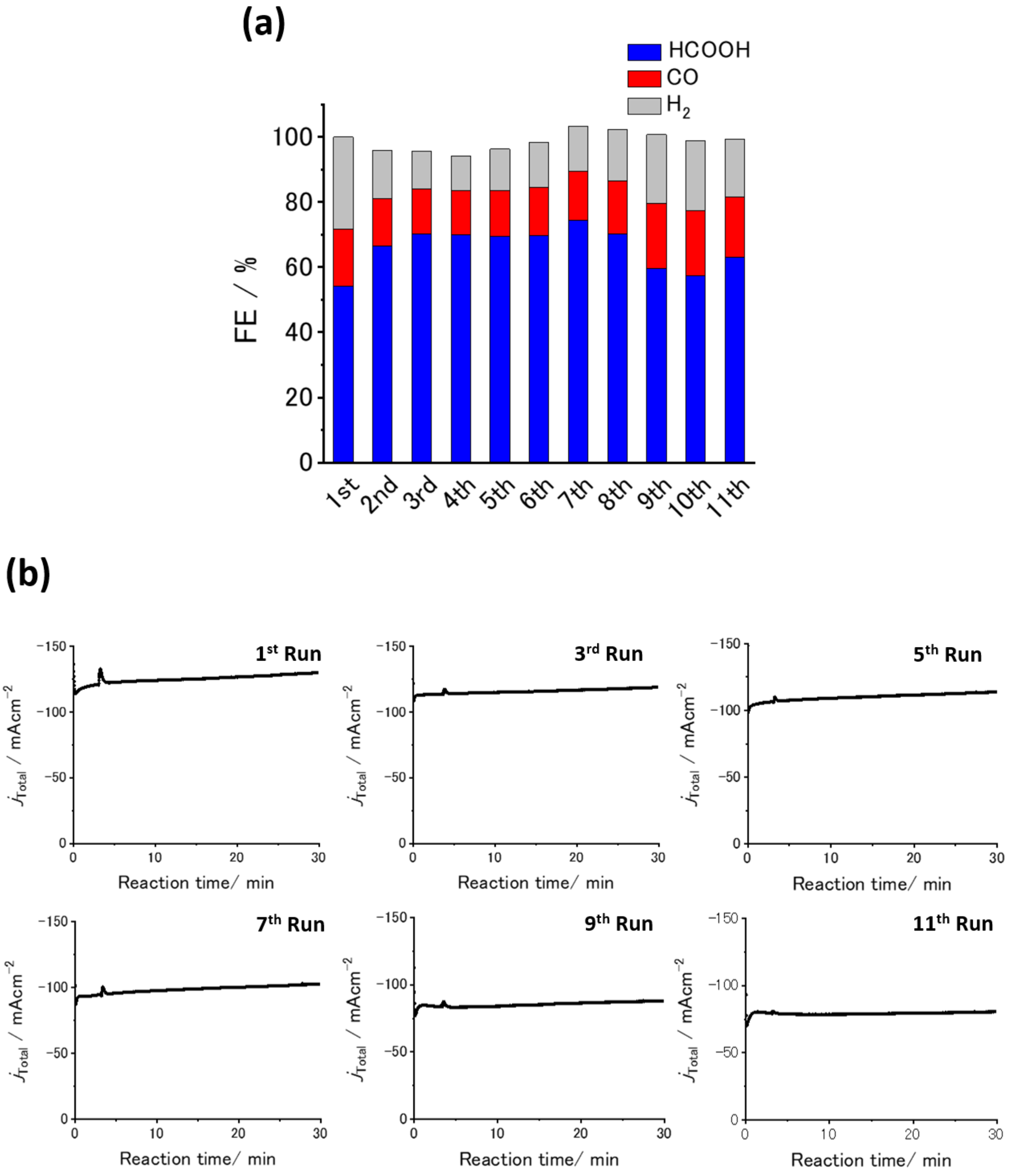

Fig. S15 (a) FE breakdown for products (b) *j*-t curves during repeated test of CO_2 electrolysis in presence of Sn-CTF/GDEs. The electrolyte (1 M $KHCO_3$(aq) (pH 8.6)) was replaced every 30 min. Potential: -2.0 V vs. RHE without IR compensation.

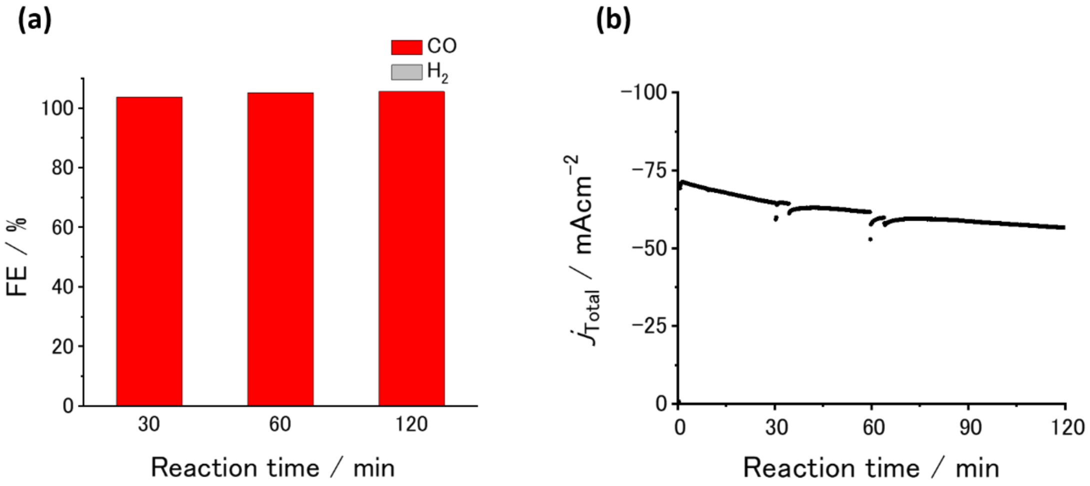

Fig. S16 (a) FE breakdown for products (b) *j*-t curves during stability test of CO_2 electrolysis for 120 min in presence of Ni-CTF/GDEs. Potential: -1.0 V vs. RHE without IR compensation; electrolyte: 1 M $KHCO_3$(aq) (pH 8.6).

The origin of a decrease in CO partial current density for Ni-CTF/GDE

A 20 % decrease in CO partial current density after 2 h was observed for Ni-CTF. Then, we consider the origin of the instability from the viewpoints of (1) degradation of catalysts and (2) flooding of GDEs.

(1) catalysts

Considering that Sn-, Co- and Ni-CTF exhibited different stability, depending on metal species, the common CTF framework itself has not been broken. In addition, although Ni bulk metal is quite active for HER,[21-23] the CO selectivity against H_2 is constant and almost 100 % even after the current decreases (Fig. S16). Therefore, the aggregation of Ni into nanoparticles can be denied. Based on these considerations, we assumed that some Ni atoms are desorbed and diffused into electrolytes during electrolysis. To verify this assumption, the Ni-CTF/GDE after the current decrease was again modified with Ni atoms by the impregnation in $NiCl_2$ solutions. As shown in Fig. S18, the partial current density of CO was recovered after the remodification of Ni atoms, supporting that the origin of the degradation of Ni-CTF was the desorption of the Ni site. We also attempted to support this consideration with the XPS measurements after electrolysis. Unfortunately, the analysis of the nickel 2*p* XPS signal on electrodes was difficult due to the spectral interference with the Auger signal of fluorine from Nafion and the low concentration of Ni atoms.[24] We will conduct a quantitative discussion by other methods in future work.

(2) flooding of GDEs

Next, let us consider the possibility of GDE flooding. There are several reports that carbonate precipitates in MPLs cause degradation. Thus, we conducted the washing tests with ultra-pure water. However, the current density was not recovered by washing the electrode with ultra-pure water (Fig. S19). Importantly, we demonstrated that the same washing process could recover the CO_2RR activity when using Cu nanoparticles as the catalysts.[25] This result revealed that the flooding of GDE would not cause a current decrease **in this time scale** for M-CTFs/GDEs. The fact that Sn-, Co- and Ni-CTF exhibited different stability, depending on metal species, also supported this consideration.

Namely, the desorption of Ni atoms from the framework mainly causes the decrease in CO partial current density in this time scale. The appropriate choice of frameworks is required to improve stability, which is ongoing in our laboratory.

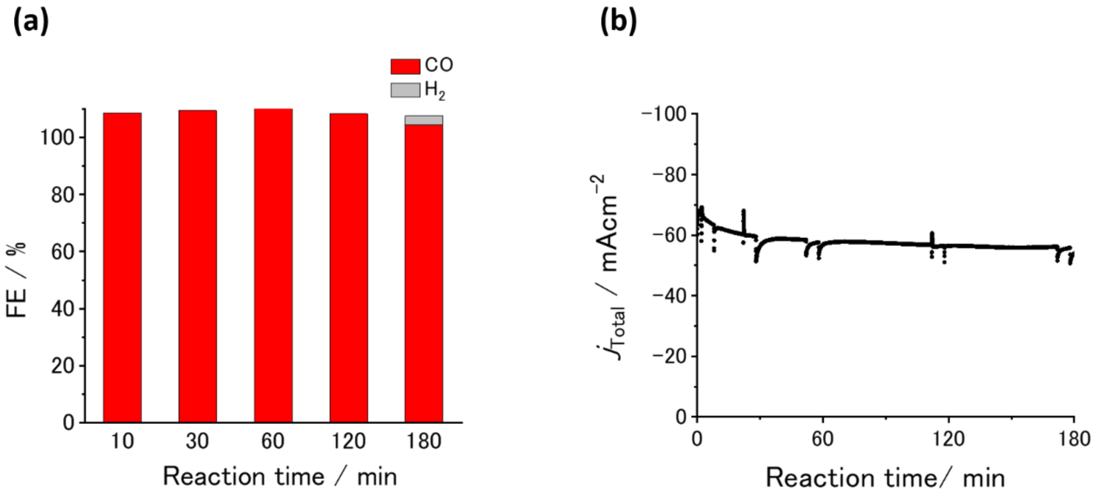

Fig. S17 (a) FE breakdown for products (b) *j*-t curves during stability test of CO_2 electrolysis for 180 min in presence of Co-CTF/GDEs. Potential: -0.8 V vs. RHE without IR compensation; electrolyte: 1 M $KHCO_3$aq.

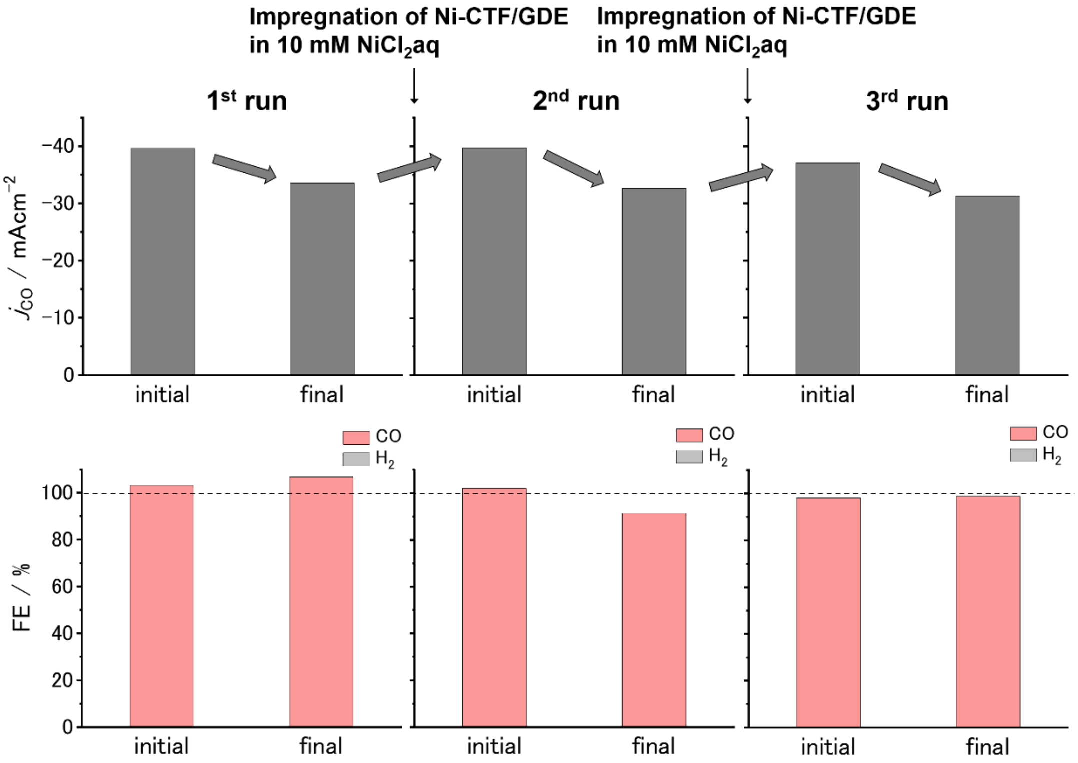

Fig. S18 Partial current density of CO generation (top) and FE (bottom) at the repeated test. After the current density decreased (at the time indicated by the thin arrows), the catalyst side of Ni-CTF/GDE was impregnated in 10 mM $NiCl_2$aq for the remodification of Ni atoms to CTF. Potential: -1.0 V vs. RHE without IR compensation; electrolyte: 1 M $KHCO_3$aq.

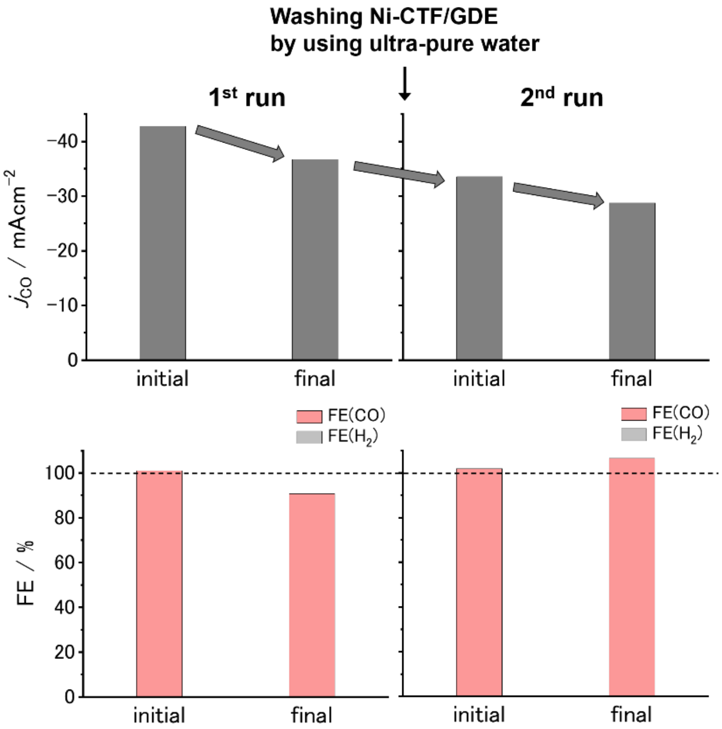

Fig. S19 Partial current density of CO generation (top) and FE for CO generation (bottom) at the washing test. After the current density decreased (at the time indicated by the thin arrows), Ni-CTF/GDE was washed with ultra-pure water by the same method used in our previous work.[25] Potential: -1.0 V vs. RHE without IR compensation; electrolyte: 1 M $KHCO_3$aq (pH 8.6).

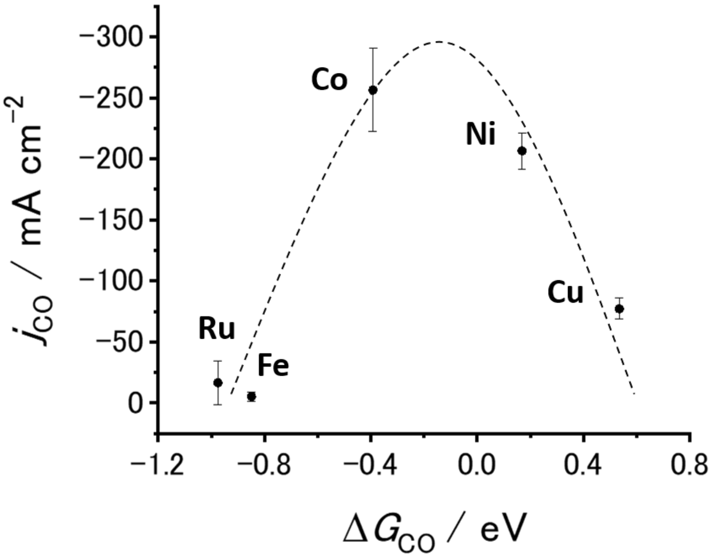

Fig. S20 Partial current density for CO generation as function of adsorption energy of CO for *M*-CTFs (*M* = Co, Cu, Ni, Fe, Ru). Potential: −0.9 V vs. RHE; electrolyte: 1 M $KHCO_3$(aq) (pH 8.6). The error bars represent the standard deviation from three experimental trials. A similar trend was observed between Fig. 6 and Fig. S20 because of the scaling relationship between ΔG(COOH) and ΔG(CO) shown in Fig. 1(c).

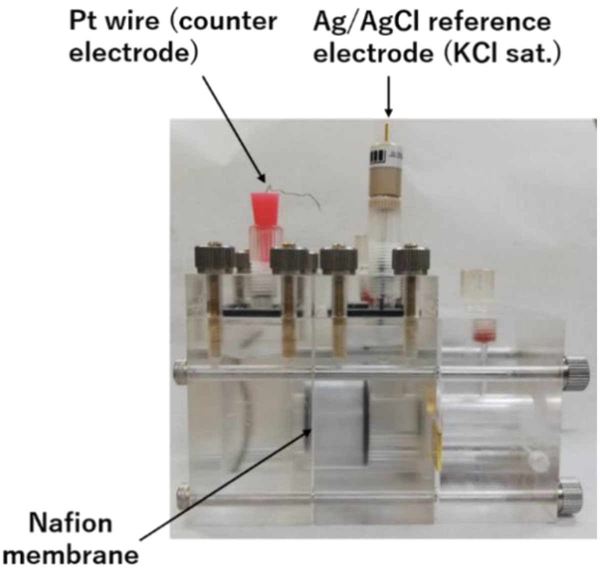

Fig. S21 Photograph of three-chamber electrochemical cell for testing GDEs.

References

1 R. Kamai, K. Kamiya, K. Hashimoto, S. Nakanishi, *Angew. Chem. Int. Ed.* 2016, **55**, 13184–13188.

2 L. N. Maskaeva, E. A. Fedorova, R. A. Yusupov, V. F. Markov, *Russ. J. Phys. Chem.* 2018, **92**, 1025–1031.

3 B. Ravel, M. Newville *J. Synchrotron Radiat.* 2005, **12**, 537-541.

4 T. Chatterjee, E. Boutin, M. Robert, *Dalton Trans.* 2020, **49**, 4257–4265.

5 T. Yamasaki, A. Kuroda, T. Kato, J. Nara, J. Koga, T. Uda, K. Minami, T. Ohno, *Comput Phys Commun* 2019, **244**, 264–276.

6 G. Kresse, D. Joubert, *Phys. Rev. B* 1999*,* **59***, 1758-1775***.**

7 J. P. Perdew, K. Burke, M. Ernzerhof, *Phys. Rev. Lett.* 1996, **77**, 3865-3868.

8 J. P. Perdew, M. Ernzerhof, K. Burke, *J. Chem. Phys.* 1996, **105**, 9982–9985.

9 A. Tkatchenko, M. Scheffler, *Phys. Rev. Lett.* 2009, **102**, 073005.

10 H. J. Monkhorst, J. D. Pack, Phys. Rev. B 1976, **13**, 5188-5192.

11 M. Methfessel, A. T. Paxton, Phys. Rev. B 1989, **40**, 3616-3621**.**

12 G. Kresse, J. Furthmiiller, *Comput. Mater. Sci.* 1996, **6**, 15-50.

13 D. M. Wood, A. Zunger, *J. Phys. A: Math. Gen.* 1985, **18**, 1343-1359.

14 P. Pulay, *Chem. Phys. Lett*. 1980, **73**, 393-398.

15 J. K. Nørskov, J. Rossmeisl, A. Logadottir, L. Lindqvist, J. R. Kitchin, T. Bligaard, H. Jónsson, *J. Phys. Chem. B* 2004, **108**, 17886–17892.

16 A. A. Peterson, F. Abild-Pedersen, F. Studt, J. Rossmeisl, J. K. Nørskov, *Energy Environ. Sci.* 2010, **3**, 1311–1315.

17 K. Ohashi, K. Iwase, T. Harada, S. Nakanishi, K. Kamiya, *J. Phys. Chem. C* 2021, **125**, 10983–10990.

18 K. Iwase, S. Nakanishi, M. Miyayama, K. Kamiya, *ACS Appl. Energy Mater.* 2020, **3**, 1644–1652.

19 S. Kattel, P. Atanassov, B. Kiefer, *J. Phys. Chem. C* 2012, **116**, 17378−17383.

20 X. Cui, W. An, X. Liu, H. Wang, Y. Men, J. Wang, *Nanoscale* 2018, **10**, 15262−15272.

21 S. Jin, Z. Hao, K. Zhang, Z. Yan, J. Chen, *Angew. Chem. Int. Ed.* 2021, **60**, 20627–20648.

22 R. Daiyan, W. H. Saputera, H. Masood, J. Leverett, X. Lu, R. Amal, Adv. Energy Mater. 2020, 10, 1902106.

23 K. Jiang, S. Siahrostami, A. J. Akey, Y. Li, Z. Lu, J. Lattimer, Y. Hu, C. Stokes, M. Gangishetty, G. Chen, Y. Zhou, W. Hill, W. B. Cai, D. Bell, K. Chan, J. K. Nørskov, Y, Cui, H. Wang, Chem, 2017, 3, 950-960.

24 S. Büchele, A. J. Martín, S. Mitchell, F. Krumeich, S. M. Collins, S. Xi, A. Borgna, J. P. Ramírez, ACS Catal. 2020, 10, 3444−3454.

25 A. Inoue, T. Harada, S. Nakanishi, K. Kamiya, EES. Catal., 2023, Advance Article, DOI: 10.1039/d2ey00035k